Geochemistry, Geophysics, Geosystems

RESEARCH ARTICLE
10.1029/2018GC008079

Key Points:
- Geodynamic and thermodynamic modeling are applied to understand the production of continental crust
- Production of continental crust produces dense residuum, which triggers Rayleigh instabilities that destabilize the lithosphere
- The continental crust production via Rayleigh-Taylor instabilities could work at low mantle potential temperature (T_P), supporting the new T_P temperatures estimates

Supporting Information:
- Supporting Information S1

Correspondence to:
A. Piccolo,
piccolo@uni-mainz.de

Citation:
Piccolo, A., Palin, R. M., Kaus, B. J.P., & White, R. W. (2019). Generation of Earth's early continents from a relatively cool Archean mantle. *Geochemistry, Geophysics, Geosystems*, *20*. https://doi.org/10.1029/2018GC008079

Received 9 NOV 2018
Accepted 9 FEB 2019
Accepted article online 19 FEB 2019

Generation of Earth's Early Continents From a Relatively Cool Archean Mantle

Andrea Piccolo[1], Richard M. Palin[2], Boris J.P. Kaus[1], and Richard W. White[3]

[1]Institute for Geosciences, Johannes-Gutenberg University of Mainz, Mainz, Germany, [2]Department of Geology and Geological Engineering, Colorado School of Mines, Golden, CO, USA, [3]School of Earth and Environmental Sciences, University of St Andrews, St Andrews, UK

Abstract Several lines of evidence suggest that the Archean (4.0–2.5 Ga) mantle was hotter than today's potential temperature (T_P) of 1350 °C. However, the magnitude of such difference is poorly constrained, with T_P estimation spanning from 1500 to 1600 °C during the Meso-Archean (3.2–2.8 Ga). Such differences have major implications for the interpreted mechanisms of continental crust generation on the early Earth, as their efficacy is highly sensitive to the T_P. Here we integrate petrological modeling with thermomechanical simulations to understand the dynamics of crust formation during Archean. Our results predict that partial melting of primitive oceanic crust produces felsic melts with geochemical signatures matching those observed in Archean cratons from a mantle T_P as low as 1450 °C thanks to lithospheric-scale RayleighTaylor-type instabilities. These simulations also infer the occurrence of intraplate deformation events that allow an efficient transport of crustal material into the mantle, hydrating it.

Plain Language Summary It has been believed that early Earth featured higher mantle temperature. The mantle temperature affects the geodynamic processes, and, therefore, the production of the continental crust, which has been a stable environment for the developing of life since Earth's infancy. However, our knowledge of the processes operating during the early Earth is still not definitive. The wide range of the mantle temperature estimation (from 1500 to 1600 °C) hampered our ability to understand early Earth's dynamic and geological data alone cannot provide a definitive answer. Therefore, it is necessary to integrate them with numerical modeling. Our contribution conjugates petrological modeling with thermal-mechanical simulations to unveil the effect of continental crust production. Continental crust's extraction from partially melted hydrated basalts leaves behind dense rocks that sink into the mantle dragging part of surface hydrated rocks. These drips produce a major compositional change of the mantle and promote the production of new basaltic/continental crust. The combination of these processes cools the mantle, suggesting that it could not have been extremely hot for geological timescales. We show that such processes can be active even in a relatively cool mantle (1450–1500 °C), providing new constraints to understand the infancy of our planet.

1. Introduction

The Earth's earliest-formed continental crust is characterized by tonalite-trondhjemite-granodiorite (TTG) (Jahn et al., 1981) that are widely accepted to have been produced via high-temperature partial melting of hydrous metabasalts (Moyen & Martin, 2012). While the geodynamic processes that formed these cratonic nuclei continue to be debated, there is a general lack of evidence for oceanic-arc/subduction-driven systems akin to those characterizing the modern Earth (Rapp et al., 2003) having dominantly operated prior to the Neo-Archean (approximately 2.8–2.5 Ga Brown & Johnson, 2018; Condie et al., 2016) or, as many authors suggested, even during the whole Archean (Bédard, 2018; Hamilton, 2007). It should be noted that Archean craton records variable processes, some of which produced features similar to Phanerozoic terrains. The geological data testify the occurrence of plate-boundary-like sequences and linear tectonic features (Kranendonk et al., 2002; Van Kranendonk, 2010). However, due to the paucity of continuum-reliable data, it is not possible to provide a definitive answer regarding the global geodynamic processes that were acting (Bédard, 2018; Bédard & Harris, 2014; Cutts et al., 2014; Van Kranendonk, 2010; Van Kranendonk et al., 2007). Archean continental crust has a dome and keel structure in which TTG batholiths intrude through overlying mafic lavas, which records a vertical reorganization of rocks as consequence of the inverse density profile (Bédard et al., 2003; Collins et al., 1998; Chardon et al., 1996). The morphology and spatial distribution of dome and keel structures in Archean terranes is inconsistent with them having formed via subduction (Bédard et al., 2003; Bouhallier et al., 1995; Chardon et al., 1996; Collins et al., 1998; Van Kranendonk, 2010). The metamorphic history of these terrain witness periods of quiescence alternating with thermal events correlating with eruption of high quantities of mafic lavas, during which the whole lithosphere was likely significantly weakened (Bédard et al., 2003; Chardon et al., 1996; Choukroune et al., 1995). Such events correlate with the remobilization of older continental crust, which undergoes partial melting to produce felsic material, alongside potential removal of lithospheric mantle (Bédard, 2006; Choukroune et al., 1995; Zegers & van Keken, 2001). Together, these observations are consistent with a tectonic setting mainly dominated by vertical tectonics, periodically fuelled by magmas derived from anomalously hot mantle sources, such as plumes (Fischer & Gerya, 2016a; Van Kranendonk, 2010). In such a scenario, continental crust would be produced via intracrustal melting and differentiation and dense mafic residua would be continuously removed via Rayleigh-Taylor instabilities (RTIs; Wiemer et al., 2018). Owing to the higher T_P, the RTIs would induce decompression melting of the asthenosphere, which would add heat to further assist continued TTG magma generation (Bédard, 2006).

The majority of Archean TTGs feature a distinctive trace element signature (e.g., high La/Yb and low Nb/Ta ratios) that requires their separation from a garnet-, hornblende-, plagioclase-, and rutile-bearing source rock (Moyen & Martin, 2012), such as garnet amphibolite or garnet granulite. These lithologies stabilize in metamorphosed mafic rock types along geothermal gradients of 900–1000 °C/GPa (Johnson et al., 2017; Palin et al., 2016). Partial melting of mafic crust must therefore have occurred at high-pressure conditions and would produce high amounts of dense residuum, which is not preserved in the Archean record. Thus, a successful geodynamic model aimed at explaining the continental crust production, must be able to predict how the mafic residuum is recycled (Bédard, 2006; Jagoutz & Kelemen, 2015; Zegers & van Keken, 2001). The geochemical signature featured by some Archean rocks resembles an arc signature, prompting the idea that the only means to transport hydrated basalts into the mantle is a subducting plate (Arndt, 2013; Van Hunen & Moyen, 2012; Wyman, 2013). Subduction models could explain how hydrous basalts are transported to great depths, providing a consistent framework to understand continental crust production. On the other hand, geological field data are more consistent with models characterized purely by vertical tectonics (Bédard et al., 2003; Chardon et al., 1998; Hamilton, 2007), which cannot replicate subduction-like geochemical features (Arndt, 2013; Moyen & Van Hunen, 2012; Wyman, 2013).

While the early Earth is known to have been hotter than today, estimates for the absolute mantle T_P during the Palaeo- to Meso-Archean (- Ga) vary from 1500 °C (Ganne & Feng, 2017) to over 1600 °C (Herzberg et al., 2010). This range is significant, as the bulk of all of the continental crust is thought to have formed during this period of time (Dhuime et al., 2012), and even small differences in mantle T_P have significant effects on the efficacy of different crust-forming processes (Gerya, 2014; Johnson et al., 2013; Sizova et al., 2010, 2014; van Hunen & van den Berg, 2008). Previous geodynamic modeling with a hot (1550–1600 °C) mantle T_P (Johnson et al., 2013) suggested that the eclogitized roots of overthickened mafic crust could have delaminated into the mantle, although they did not consider TTG generation in the same environment. Other numerical studies addressing crust-forming processes did not explore the effect of variable T_P and have not examined changes in composition and density of the mafic crust during partial melting and melt extraction (Fischer & Gerya, 2016a; Rozel et al., 2017; Sizova et al., 2015). Although such studies have predicted the unstable nature of the lithosphere at high mantle T_P, they did not explore the effect that magmatism has on thermal weakening of the lithosphere, but instead considered a lithosphere prone to be delaminated and gravitationally unstable (e.g., Fischer & Gerya, 2016a, and Sizova et al., 2015, employed a high initial crustal Moho temperature that implies a weak lithosphere).

Here we employ a new generation of integrated petrological and thermomechanical models to examine the effect of variable mantle T_P on the mineral assemblages produced during heating and thickening of Archean mafic crust, the geochemistry of derivative partial melts, and the removal of crustal melt-depleted residua (see Figure 1). This modeling replicates a magmatic-dominated geodynamic environment, which is thought to have characterized the preplate tectonic Earth (Cawood et al., 2013; Fischer & Gerya, 2016a), and likely involved repeated internal restructuring via cyclical RTI events (Collins et al., 1998; Fischer & Gerya, 2016a; Johnson et al., 2013; Sizova et al., 2015).

10.1029/2018GC008079

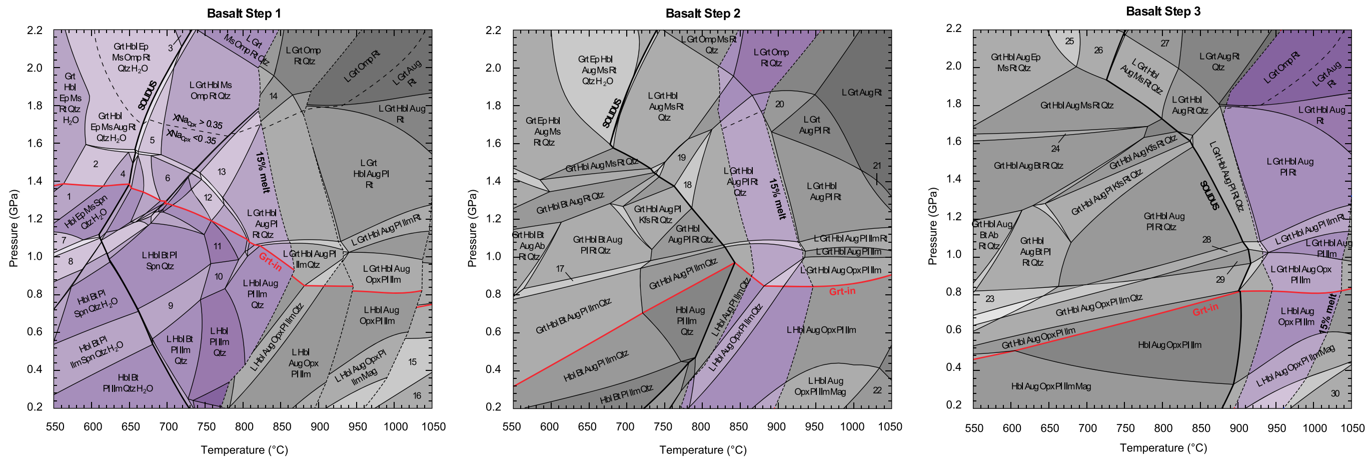

Numbered Field: *1 – Brs Ep Ms Spn Rt Qtz H2O; 2 – Grt Brs Ep Ms Spn Rt Qtz H2O;3 – Grt Hbl Ms Omp Rt Qtz H2O;4 – Grt Brs Ep Ms Spn Qtz H2O;5 – L Grt Brs Ep Ms Omp Rt Qtz; 6 – L Grt Brs Ms Omp Spn Qtz; 7 – Hbl Ep Bt Ms Spn Qtz H2O 8 – Hbl Bt Ms Spn Ab Qtz H2O; 9 – L Hbl Bt Pl Ilm Spn Qtz; 10 – L Hbl Pl Ilm Spn Qtz; 11 – L Hbl Pl Spn Qtz; 12 – L Grt Hbl Aug Kfs Pl Spn Qtz; 13 – L Grt Hbl Aug Kfs Pl Rt Qtz; 14 – L Grt Hbl Di Rt Qtz; 15 – L Hbl Di Opx Pl Ilm Mag 16 – L Hbl Di Opx Pl Mag; 17 – Grt Hbl Bt Aug Pl Ilm Rt Qtz; 18 – L Grt Hbl Aug Pl Kfs Rt Qtz; 19 – L Grt Hbl Aug Kfs Rt Qtz; 20 – L Grt Aug Pl Rt Qtz; 21 – L Grt Hbl Aug Rt; 22 – L Hbl Aug Pl Ilm Mag; 23 – Grt Hbl Aug Bt Pl Qtz; 24 – Grt Hbl Aug Ms Bt Rt Qtz; 25 – Grt Hbl Aug Ep Ms Rt Qtz H2O; 26 – Grt Hbl Aug Ms Rt Qtz H2O; 27 – L Grt Aug Ms Rt Qtz; 28 – Grt Hbl Aug Pl Rt Ilm Qtz; 29 – Grt Hbl Aug Opx Pl Rt Ilm Qtz; 30 – L Hbl Pl Aug Mag*

Figure 1. The purple area in each phase diagram represents the phase relation that can be seen by a rock during a prograde metamorphic between the solidus and the 15% melt modal amount.The red line represents the garnet-in boundary. The leftmost picture represents the first basalt step (BS1), the most fertile and hydrated rock. The middle one represents the second basalt step (BS2), while the rightmost is the last basalt step (BS3), which is used also for anhydrous intrusions.

2. Methods

2.1. Geodynamic Simulations

The geodynamic simulations used a Lagrangian thermomechanical finite-element code MVEP2 (Johnson et al., 2013; Thielmann & Kaus, 2012), which solves the 2-D fundamental continuum mechanics equations using a extended Boussinesq approximation. The advection of material properties within the numerical domain is handled by a marker-in-cell technique. The fundamental equations are

$$\frac{\partial v_i}{\partial x_i} = 0, \tag{1}$$

where v is the velocity vector,

$$\frac{\partial \tau_{ij}}{\partial x_j} - \frac{\partial P}{\partial x_i} = -\rho g_z, \tag{2}$$

where P is pressure, τ_{ij} is the deviatoric stress component along the considered direction, ρ is density, and g_z is the gravity vector component ($g_z = 9.81$ m/s^2).

$$\rho C_p \left(\frac{\partial T}{\partial t} + v_i \frac{\partial T}{\partial x_i} \right) = \frac{\partial}{\partial x_i} \left(K \frac{\partial T}{\partial x_i} \right) + H_a + H_s + H_r + H_l, \tag{3}$$

$$H_s = \tau_{ij} \left(\dot{\epsilon}_{ij} - \dot{\epsilon}^{el}_{ij} \right), \tag{4}$$

$$H_a = T \alpha v_z g, \tag{5}$$

C_p is the heat capacity, T is the temperature, and K is the heat conductivity, which is a function of temperature, pressure, and composition (Sizova et al., 2015). H_r, H_s, H_l, and H_a are radiogenic heat production, shear heating (equation (4)), latent heat, and adiabatic heating (equation (5)), respectively. Latent heat is considered for the melt reactions and is handled by changing the heat capacity and thermal expansivity as function of the melt production (e.g., Sizova et al., 2015):

$$\alpha_{eff} = \alpha + \frac{\rho Q_l}{T} \left(\frac{\partial M}{\partial P} \right), \tag{6}$$

$$C_{peff} = C_p + Q_l \left(\frac{\partial M}{\partial T} \right), \tag{7}$$

where α_{eff} and C_{peff} are the effective thermal expansivity and heat capacity of the partially melted rock, respectively. Q_l is the latent heat. While heat conductivity changes accordingly to an empirical law (Clauser & Huenges, 1995),

$$K(X,P,T) = \left(k_1 + \frac{k_2}{T + 0.77}\right)\exp(Pk_3), \tag{8}$$

where k_1, k_2, and k_3 are empirical parameters that describe how the conductivity changes as function of pressure and temperature (see Table S1 in the supporting information).

2.1.1. Rheological Model

MVEP2 is a viscoelastoplastic code. As a consequence, the deviatoric stress tensor is computed using three constitutive equations that connect it with the strain rate tensor;

$$\dot{\epsilon}_{ij} = \dot{\epsilon}_{ij}^{\text{vis}} + \dot{\epsilon}_{ij}^{\text{el}} + \dot{\epsilon}_{ij}^{\text{pl}} = \frac{\tau_{ij}}{2\eta_{\text{eff}}} + \frac{\diamond\tau_{ij}}{2G} + \dot{\gamma}\frac{\partial Q}{\partial \tau_{ij}}, \tag{9}$$

where $\dot{\epsilon}_{ij}$ is the total strain rate tensor, the superscript el, vis, and pl indicate respectively the elastic, viscous, and plastic strain rate; $\diamond\tau_{ij}$ is the Jaumann objective stress rate, and G is the shear modulus; η_{eff} is the effective viscosity; $\dot{\gamma}$ is the plastic multiplier; Q is the plastic flow potential, which is equal to the second invariant of the deviatoric stress tensor, in a dilatation-free media (Kaus, 2010). We briefly describe the method and numerical implementation, which is explained in more detail in Kaus (2010). The creep viscosity was computed using the following equations from Hirth and Kohlstedt (2004):

$$\eta_{\text{diff}} = A_{\text{diff}}^{-1} d^p \exp\left(\frac{E_{\text{act}} + PV_{\text{act}}}{RT}\right)\exp(AM), \tag{10}$$

$$\eta_{\text{disl}} = A_{\text{disl}}^{-\frac{1}{n}} \dot{\epsilon}_{II}^{\frac{1}{n}-1} \exp\left(\frac{E_{\text{act}} + PV_{\text{act}}}{nRT}\right)\exp\left(\frac{AM}{n}\right). \tag{11}$$

A_{diff} and A_{disl} are the preexponential factors for diffusion and dislocation, respectively (see Table S1), d and p are the grain size and the grain size exponent, respectively, and n is the stress exponent. E_{act} and V_{act} are the activation energy and activation volume. A is an empirical parameter that describes the porosity weakening associated with melt production, and M is the actual volumetric degree of melt after the melt extraction; $\dot{\epsilon}_{II}$ is the second invariant of the strain rate tensor (all parameters used are listed in Table S1). The effective viscosity (η_{eff}) is computed with a quasi-harmonic average between diffusion and dislocation creep viscosity. Brittle rheology was modeled using a Drucker-Prager yield criteria:

$$F(\tau_{II}) = \tau_{II} - C\cos(\phi_{\text{dry}}) - P\sin(\phi_{\text{dry}})\lambda_{\text{melt}}, \tag{12}$$

$$\lambda_{\text{melt}} = 1 - \frac{P_f}{P_l}. \tag{13}$$

F is the yield function, C the cohesion of the material, and ϕ is the dry friction angle; λ_{melt} is the weakening factor induced by the melt phase percolating within the rocks during the melt extraction.

At the beginning of the time step, F is assumed ≤ 0, which implies that the plastic deformation mode is not active:

$$\dot{\lambda} \geq 0, F \leq 0, \dot{\lambda}F = 0. \tag{14}$$

The numerical code computes trial stresses using a viscoelastic rheology, after which the resultant stresses are used to compute $F(\tau_{II})$:

$$\tau_{ij} = 2\eta_{ve}(\dot{\epsilon}_{ij}) + \chi\tau_{ij}^{\text{old}} \tag{15}$$

with

$$\chi = \left(1 + \frac{G\Delta t}{\eta_{\text{eff}}}\right)^{-1}, \tag{16}$$

$$\eta_{ve} = \left[\frac{1}{\eta_{\text{eff}}} + \frac{1}{\Delta t G}\right]^{-1}, \tag{17}$$

where τ_{ij}^{old} is the deviatoric stress of the previous time step and Δt is the current time increment. If $F(\tau_{ij})$ is >0, the code computes a plastic strain rate as such the trial stresses become equal to the stresses predicted by the yield criteria:

$$\tau_{ij} = 2\eta_{ve}(\dot{\epsilon}_{ij} - \dot{\epsilon_{ij}}^{pl}) + \chi\tau_{II}^{\text{old}}. \tag{18}$$

Equation (18) can be rearranged:

$$\tau_Y = 2\eta_{vep}\dot{\epsilon}_{II} + \chi\tau_{II}^{\text{old}} \tag{19}$$

yielding an effective viscosity:

$$\eta_{\text{vep}} = \left(\frac{\tau_Y - \chi\tau_{II}^{\text{old}}}{2\dot{\epsilon}_{II}}\right), \tag{20}$$

where $\dot{\epsilon}_{ij}^{pl}$ is the plastic strain rate, τ_Y is the yield stress, and η_{vep} represents an effective viscosity resulting from all the three deformation mechanisms. If the rock is not yielding, the effective viscosity is given by equation (17), otherwise is given by equation (20).

The effective viscosity can vary between a lower and upper threshold values of 10^{18} and 10^{24} Pa·s, respectively. If the effective viscosity yielded by equation (16) is outside this range, it is automatically set equal to the lower or upper bound. This strategy, which is common for all geodynamic software packages, is imposed for numerical stability as roundoff errors can affect the performance and accuracy of the direct solvers.

2.2. Petrological Modeling and Melt Extraction

2.2.1. Melt Extraction

The extraction of melt from each source rock and its emplacement are assumed to be instantaneous over the timescales considered in the geodynamic model, although these processes operate at different rates in the natural environment. While the rate of crystallization for intrusive rocks was modeled according to pluton size, the crystallization of volcanic rocks was considered instantaneous (cf. Sizova et al., 2015). At each time step, the melt quantity is interpolated from the phase diagrams (M^E). The interpolated value, however, does not incorporate the extraction event that occurred between two depletion steps. To avoid any melt overproduction, we correct the value using the previously melt extracted, yielding an effective melt quantity ($M*$):

$$M* = M^E - \sum_{i=1}^{ts-1} M_{\text{ext}}(i). \tag{21}$$

M_{ext} is the volume of melt that has migrated from the source during each extraction event, and ts is the total number of extraction events.

After the computation of $M*$, the code tests whether if this value is higher than $M1$, which represents the minimum melt fraction above which melt can escape from the source. This value is the numerical expression of the critical amount of melt in high-pressure metabasic rocks (Rushmer, 1995). Since the critical amount of melt depends on the deformation, geometric configuration of the minerals, and reaction rates, we use a constant value that is varied within the simulations. As a consequence, we neglect some real-world complexities. There are two cases: $M^* < M1$ and $M^* \geqslant M1$. In the first case, M, the effective amount of melt used in the equations (11) and (10) and in the density computation (see below) is $M = M^*$ and $M_{\text{ext}} = 0$, in the latter $M = M2$ and $M_{\text{ext}} = M^* - M2$. $M2$ is the minimum amount of melt that remains in the source, which controls melt-driven viscous weakening and the buoyancy of the media after melt extraction. As with $M1$, $M2$ depends on many factors that cannot be easily parameterized, and for simplicity, we set it as a variable input parameter. After each extraction event, all particles are vertically compacted, reproducing the mass and volume change of the source rocks. After the current melt extracted is computed for each node, we sum the contribution along z direction, yielding an effective thickness of extracted material. This effective thickness is used to apply a compaction to the particles, which creates space for newly generated crust.

The volume of extracted melt is converted into extrusive or intrusive crust, whose proportion is defined by the parameter I_R ($= V_{\text{intrusion}}/V_{\text{Totmelt}}$), which is an nondimensional quantity that ranges from 0 to 1 (0% to

10.1029/2018GC008079

100%). The intrusion is emplaced where the maximum ratio between the fluid overpressure and effective viscosity is achieved:

$$div(C) = \frac{P_{\text{liquid}} - P_{\text{solid}}}{\eta_{\text{eff}}}. \quad (22)$$

P_{liquid} is the hydrostatic liquid pressure computed accordingly to the melt density, while P_{solid} is the lithospheric pressure. The depth of emplacement depends on the density of the melt and on the rheology of the crust, and it changes according to the dynamics of the system.

2.2.2. Petrological Modeling

Petrological modeling of metamorphism and partial melting in Archean crust was performed in the Na_2O-CaO-K_2O-FeO-MgO-Al_2O_3-SiO_2-H_2O-TiO_2-O_2 system using *THERMOCALC* version 3.45i (Powell & Holland, 1988), internally consistent thermodynamic data set ds62 of Holland and Powell (2011), and the following *ax* relations: epidote, olivine (Holland & Powell, 2011), silicate melt, augite, hornblende (Green et al., 2016), garnet, orthopyroxene, biotite, chlorite (White et al., 2014), magnetitespinel (White et al., 2002), ilmenitehematite (White et al., 2000), Cbar-1 plagioclase, K-feldspar (Holland & Powell, 2003), and muscoviteparagonite (White et al., 2014). All calculations utilized the initial bulk rock composition for an average large-ion lithophile element-enriched Archean tholeiite (EAT, Condie, 2003), which has been suggested on major- and trace-element geochemical grounds to be the most suitable source rock for Archaean TTGs (Martin et al., 2014; Moyen & Martin, 2012).

The bulk chemical composition of a rock imparts a primary control on the phases that stabilize as a function of *PT* conditions, solidus topology, and ultimately on their rheology, density, and radiogenic heat productivity. All together, these effects have first-order controls on the dynamics of the target system. To encompass such complex feedback, we parameterized the chemical evolution of the rocks by discretizing it, and assuming that it compositionally evolves only as function of melt loss. We averaged the chemical composition of the residuum along the same melt-fraction isoline to produce new phase diagrams. Such chemical evolution is matched to individual particles that carry all petrophysical information and are advected within the numerical domain.

All particles have their own identification number and rock type. Rock type connects the particles with the petrothermochemical properties of the modeled lithotype and with phase diagrams. To enforce the chemical composition evolution, the rock type of a particles can change if the total melt extracted exceeds a threshold value, $M3$ (see below and supporting information Figure S12). We do not explicitly deal with reaction lines; the residual composition and associated phase diagram is computed beforehand (see below for further details). Albeit more sophisticated and correct methods exist and have been already applied (Riel et al., 2018; Rummel et al., 2018), they require more computational cost and resources that make them currently unsuitable for obtaining statistically significant results for the Archean dynamics. Radiogenic heat productivity is assumed to diminish at each depletion step, and it discretely varies within an interval whose extremes are the inferred Archean and the modern-day values for the respective lithologies (e.g., mantle radiogenic heat production interval spans from 0.022 to 0.066 μW/m^3 and each evolutionary stage entails a decrease of 0.022 μW/m^3). Petrophysical properties of metamorphic rock types, such as whole rock density, individual melt and residuum density, volumetric melt fraction (M^E), and constituent mineral compositions and proportions, were calculated using *THERMOCALC* and used as input data for geodynamic modeling. Given that melt loss is an open-system process, M^E was adjusted during each extraction event; consequently, this value differs from M (effective volumetric degree of melt). A unique phase diagram was thus calculated for each rock type (e.g., basalt step 4 [BS4] and mafic intrusion). All petrophysical properties of unmelted protolith, extracted melt, and depleted residuum (e.g., density) were calculated for each node as a function of pressure, temperature, composition (X), and M:

$$\rho_{\text{eff}}(X, P, T, M) = M\rho_{\text{melt}}(X, P, T) + (1 - M)\rho_{\text{solid}}(X, P, T), \quad (23)$$

where $\rho_{\text{melt}}(X, P, T)$ is the density of the melt and $\rho_{\text{solid}}(X, P, T)$ is the density of the solid fraction. Since we do not consider continental crust reworking, we do not use phase diagrams for the felsic crustal rocks, and its density is computed by using a simple parameterization:

$$\rho_{\text{felsic}}(P, T) = \rho_0 \left[1 - \alpha(T - T_0)\right] \left[1 + \beta(P - P_0)\right], \quad (24)$$

Table 1
Composition of Basalts Used in Geodynamic Models From Which TTG Magmas Were Derived All the Compositions Are Listed as Mole Percent Oxide

Rock types	H_2O	SiO_2	Al_2O_3	CaO	MgO	FeO^{Tot}	K_2O	Na_2O	TiO_2	O
BS1/BT2	6.830	49.693	8.992	9.214	10.205	9.814	0.442	2.628	1.125	1.058
BS2	4.443	47.975	9.118	10.330	11.775	11.238	0.227	2.373	1.304	1.226
BS3	2.329	45.712	9.198	11.557	13.489	12.738	0.102	1.947	1.509	1.419
BS4(*)	1.163	43.856	9.173	12.879	14.824	13.380	0.044	1.284	1.751	1.647

Note. (*) BS4 has the same phase diagram of BS3, but, after the extraction, the predicted composition is the one listed. BS1 = basalt step 1; BS2 = basalt step 2; BS3 = basalt step 3; BS4 = basalt step 4; BT2 = basalt type 2.

where ρ_0 is the reference density (2,650 kg/m^3), T_0 and P_0 are respectively the reference temperature and pressure.

The initial mafic crust was assumed to be large-ion lithophile element-enriched Archaean tholeiite (EAT) derived from a primitive undifferentiated dry mantle (Condie, 2005). Phase diagrams were calculated for specific bulk rock compositions depending on the number of times that melt had been extracted, as follows:

1. Mantle rocks: Phase equilibria for the asthenospheric mantle source rock were calculated using the fertile peridotite (MFP) composition presented by Johnson et al. (2013)—the *ax* relations and thermodynamic data sets are outlined therein—and a total melt extraction threshold of 25% (i.e., $M3 = 25\%$) was applied. Following melt loss, the complementary effective bulk composition for lithospheric mantle (also taken from Johnson et al., 2013) was termed *mantle depletion step* 1 (MDS1). During our systematic analysis, the rheological flow law of MFP was changed to simulate stiffening of the mantle as consequence of melt extraction. The stiffening of the mantle is modeled by increasing the preexponential factor of diffusion and dislocation creep by 1 order of magnitude (see Table S2 for further information). MDS1 was allowed to melt, and if the incremental melt extraction exceed 45% of total melt extracted the rock type and phase diagram was changed for the last time; MDS2 was not allowed to melt again, meaning that no further chemical evolution of the mantle took place in our model.
2. Crustal rocks: Phase equilibria for mafic crustal units were computed using *THERMOCALC* 3.45 (Powell & Holland, 1988), using the Holland and Powell (2011) data set (ds62) and the *ax* relations of Green et al. (2016) as outlined above (see Figure 1). A phase diagram for undepleted EAT (BS1) was utilized as a baseline reference system from which subsequent pseudosections were derived. A melt-extraction threshold (M3) of 15% was applied for these crustal lithologies (following Rushmer, 1995) , with sequential melt loss producing increasingly depleted source rocks and melts termed basalt step 2 (BS2), basalt step 3 (BS3), and BS4 (Palin et al., 2016), the last of which has an anhydrous residue and thus no longer produces significant quantities of melt. Bulk compositions for melt-depleted lithologies were calculated using the read-bulk-info matrix function, which was adjusted to account for 15% relative melt loss at the *PT* conditions of melt extraction calculated on the 15% melt proportion contour from the source lithology. This threshold was chosen owing to it representing the upper limit of favorable conditions for efficient melt segregation and escape from partially melted mafic rocks, as determined experimentally for garnet amphibolites by Rushmer (1995). While such a value is affected by several factors (i.e., strain, temperature, grain size, and shape), it represents a defensible cutoff for the lithologies and general *PT* conditions of melting observed in this simulation, which match those used during the experiments of Rushmer (1995).

Phase diagrams for residual lithotypes used these critical melt fractions, within the perspective of minimizing the number of phase diagrams to be discretized while being able to capture the first-order effect of the chemical composition evolution. We use a lower melt threshold ($M1$) to incorporate all kinds of magmatic processes that may occur during the extraction. All melts generated are termed felsic and either erupt as lavas or stall as intrusions in the middle to lower crust. These felsic melts can be derived from BS1, BS2, BS3, or basalt type 2 (BT2). The bulk compositions used for modeling are given in Table 1. The effusive basalt associated with the mantle phase MDS1 has a different composition, but it is modeled using the same phase diagrams of the BS1 as most metabasalts have similar melting evolution (Palin et al., 2016). We differentiate it from the other kind of basalts (BT2) to track the amount of basalt coming from a depleted mantle source. It produces small amount of felsic melt and then is converted into a dense residue without following the path assigned to the EAT basalts. In any case the amount of BT2 is negligible respect to the EAT protoliths, as it does not contribute significantly to overall felsic magma production.

In each time step, both intrusive and effusive crust is produced by the mantle-derived melts. Intrusive mafic systems are complex and feature internal differentiation, producing composite suites of rock dominated by dry gabbro and ultramafic cumulates (Cox, 1980). Such complexity cannot be handled by the current melt extraction parameterization. Therefore, we choose to simplify it introducing an effective dense unfertile material that is emplaced as intrusive body within the lower crust or as underplated mafic materials. We assume that these composite intrusions feature a high magnesium number and to model these dense bodies, we employ the same phase diagram of the BS3, without melting, of which composition resembles Archean picrites. Intrusion as possible source of the felsic crust was not considered to avoid overestimation of felsic material and preferring to investigate the effects of the evolution of the hydrous mafic crust. In previous work (Sizova et al., 2015), the dry underplated basalt have been considered as available source of felsic crust as well. However, the bulk of continental crust produced in their simulation were originated by dry intrusions, and it has been interpreted as intermediate material (i.e., andesite). However, intermediate rocks are rare in the Archean terrains (Anhaeusser, 2014), and we choose to focusing only in the mafic protolith that could really bear TTGs. However, the density of these intrusion is higher than a normal dry basalt, so in order to check if the prediction of such approach is correct, we performed a test using the anhydrous basalt employed in Johnson et al. (2013), yielding a similar results.

Our approach has an important limitation related to the dehydration reactions. Our modeling approach cannot handle the dehydratation reaction and the magmatic processes. All the mafic crust phase diagrams have computed assuming that the BS1 is always minimally saturated in water at the solidus. This approach guarantees that the rocks were always saturated during the prograde metamorphism, and it implicitly assumes that the rocks are always fully hydrated. In any case, with the exception of perfectly anhydrous metabasalt, all partially or fully hydrated metabasalts will produce the majority of their melt at similar conditions across the amphibolite-to-granulite boundary (Palin et al., 2016). So, our numerical experiments represent the most favorable conditions to produce continental crust in a vertical setting.

In summary, the compositional evolution starts with an MFP that melts as consequence of the increase of T_P due to mantle radiogenic heat production and decompression. After 25% of melt extracted, the mantle fertile peridotite evolves toward the MDS1, which could produce new basalts with different composition (BT2). If the MDS1 and the initial lithospheric mantle experience 20% melt extraction, it is converted into MDS2 and is considered fully depleted. The product of MFP is dense mafic intrusion (Intrusion) and tholeiitic basalts (basalt step 1 [BS1]). The hydrated basalt is buried and heated from below, and if it melts, it generates high silica melt, that is extracted generating Felsic Crust. BS1 evolves toward the BS2 (after 15% melt extraction), which eventually melts again producing new felsic crust and evolving toward the BS3 and then to BS4. If total melt extracted is higher than the respective threshold (15%, 30%, and 45%, respectively) the phase diagram and rock type are changed.

2.3. Results

2.3.1. Initial Setup

Our baseline scenario (reference model) is represented by a two-dimensional numerical model comprising numerous layers (see supporting information [Gerya & Meilick, 2011; Gerya et al., 2008; Kaus et al., 2010; Ranalli, 1995], Figure S1). With increasing depth, this comprised an 80-km-thick lithosphere with a 24-km-thick crust, of which the uppermost portion is composed of 16 km of hydrated (fertile) basalts (BS1) overlying 8 km of anhydrous (unfertile) basalt/gabbro (Intrusion). The underlying lithospheric mantle is considered partially depleted, consistent with the predicted Archean residual mantle composition (Johnson et al., 2013; Herzberg et al., 2010). The asthenospheric mantle is composed of anhydrous MFP. The mineral assemblages (with or without melt) that would be stable at each PT conditions through this profile were calculated using thermodynamic phase equilibrium modeling (see section 2), alongside bulk rock physical properties (e.g., density). These phase assemblages dynamically evolved with simulation time and were recalculated at each node as P, T, and bulk composition constraints changed.

The lithosphere featured an initially segmented geotherm: a crustal segment, with a Moho temperature (T_{Moho}) of 800 °C, which produced an apparent geotherm of 1000 °C/GPa, and a lithospheric mantle segment, with a T_P at the base of the lithosphere of 1550 °C. This reference model assumes effective melt weakening ($\lambda_{\mathrm{melt}} = 0.01$), which reduces the brittle strength of the lithosphere during melt-loss events

10.1029/2018GC008079

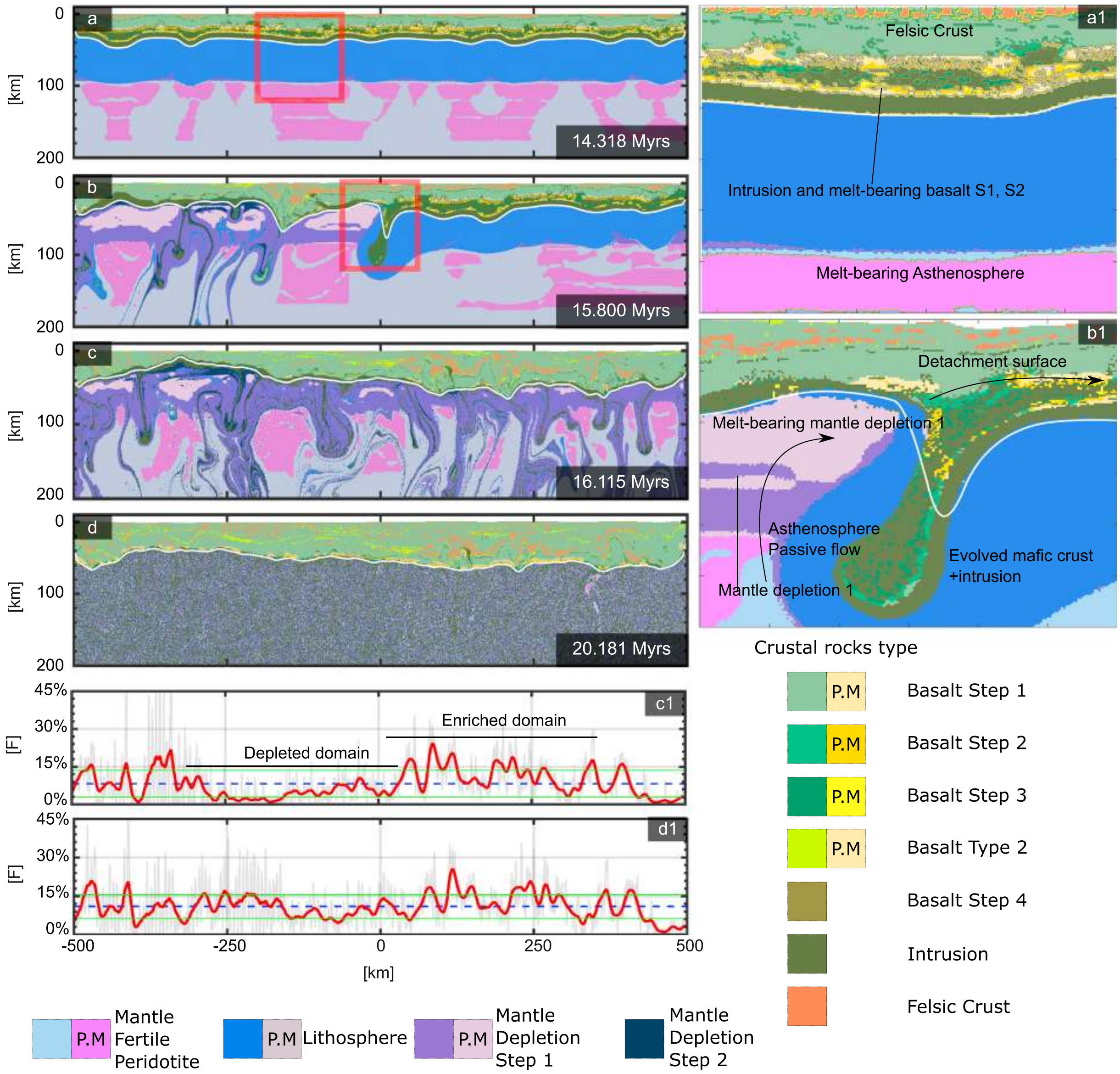

Figure 2. Temporal evolution of the reference simulation ($T_P = 1550\,°C$, $T_{Moho} = 800\,°C$, $\lambda_{melt} = 0.01$, $\phi_{dry} = 30°$, and an intrusive/extrusive ratio = 50%. Three characteristic evolutionary stages are shown: (a) incubation, (b, c) dripping and intraplate deformation substage, and (d) steady state stage. (a1) and (b1) are related respectively to (a) and (b) and are enlargement of the area surrounded by the thick rectangular boxes. (c1) and (d1) are the monodimensional profile, in which F, the relative amount of felsic crust, is plotted against the horizontal direction. The red line is the moving average of the raw data—gray lines in the same plot—with a window of 20 km, the blue line represents the global average, and the two green lines represent one standard deviation of the data.

(Sizova et al., 2015). As the hydrated basalts (BS1) are buried, they partially melt, with phase equilibrium modeling used to calculate the compositions of generated magmas. Such melts are high-silica magmas that can be extracted to form felsic crust (see section 2). Once the calculated volume of melt generated reaches a critical threshold, accumulated melt is extracted from the system. As this changes the bulk composition of the system, a new phase diagram was calculated to determine the stable mineral assemblage following melt loss (see Figure 1). Such stepwise melt-loss and depletion was permitted to occur up to three times, such that melt was extracted from each basalt when its cumulative total reached 15%, after which the rock is considered fully melt-depleted (BS1–BS4). Likewise, the asthenospheric mantle was allowed to change phase diagrams two times when the total melt extracted reached the two thresholds values (25% and 45%). These stages are denoted MFP to MDS1 and MDS2. Extracted melt is either converted into hydrated basalt (BS1) if extruded, consistent with an Archean subaqueous environment (Kump & Barley, 2007) or as anhydrous basalt/gabbro if intruded.

10.1029/2018GC008079

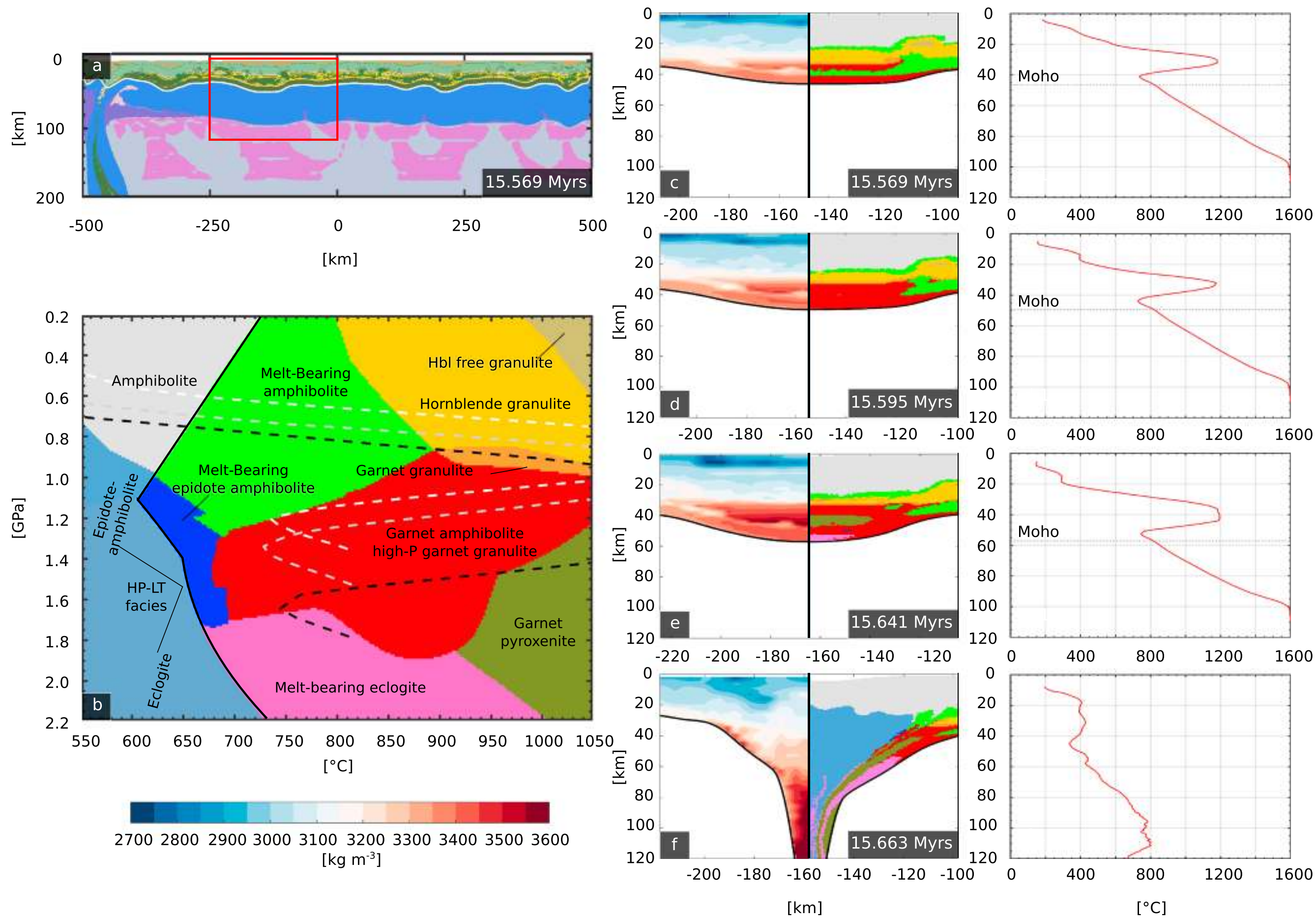

Figure 3. Petrophysical architecture of a drip. (a) The reference scenario in the embryonic stage of drip formation. (b) Petrological diagram showing rock types stable at different pressure-temperature conditions within the drip, taken from Palin et al. (2016). Color coding for rock type is used for subsequent plots. The dashed lines represent the geotherm along the axis of the drip (white, gray, and black refer, respectively, to panels c–e). (c) Embryonic predrip stage when intrusion of magma begins to heat the lower crust. Rock types at this depth are dominantly amphibolite and garnet amphibolite and have densities of around 3200–3400 kg/m^3. (d) Densification of lower crustal units occurs soon after initial drip embryo development. The density of the lower crust is increased with respect to the mantle, due to mafic residue left over from extraction of felsic crust. (e) Minor eclogite-facies rocks form at the base of the crust as a result of thickening and drip development. (f) Dripping eventually occurs owing to gravitational instability.

MDS1 produces small amounts of melt that generate a distinct basalt (BT2) to highlight the difference between the basalt that is produced from a more fertile source with respect to those produced by a partially depleted one. BT2 undergoes a single stage before being converted in unfertile residue (see section 2). Initially, 50% of the mafic melt produced was assumed to stall during ascent through the crust and form intrusions. While this is lower than the average noted for the present-day Earth (80–90% intrusion; Crisp, 1984), this ratio is highly variable between geological environments; for example, plume-related magmatism is typically characterized by 66% of magmas forming intrusions (Crisp, 1984; White et al., 2006), and this ratio can evolve with time depending on the rheological structure of the crust changing during cooling (Rubin, 1993). In our modeling, extrusion is assumed to occur via dike formation, with the diking efficiency controlled by the rheological structure of the crust (Rubin, 1993). In most simulations, we employ a conservative scenario in which the eruptive efficiency remains constant throughout the simulation, which mimics stiffening of the crust due to eruption of high amounts of mafic lavas (Rubin, 1993). This ratio produces a strong crust, which promotes diking and efficient effusive volcanism, consistent with the thick volcano-sedimentary sequences in Paleo-Archaean terrains (e.g., the East Pilbara craton Hickman & Van Kranendonk, 2012).

2.3.2. Reference Model

The reference model exhibited three main stages: an incubation stage; a drip stage, which features strong intraplate deformation; and a steady state stage (Figure 2). During the *incubation stage* (0–14 Myr), the

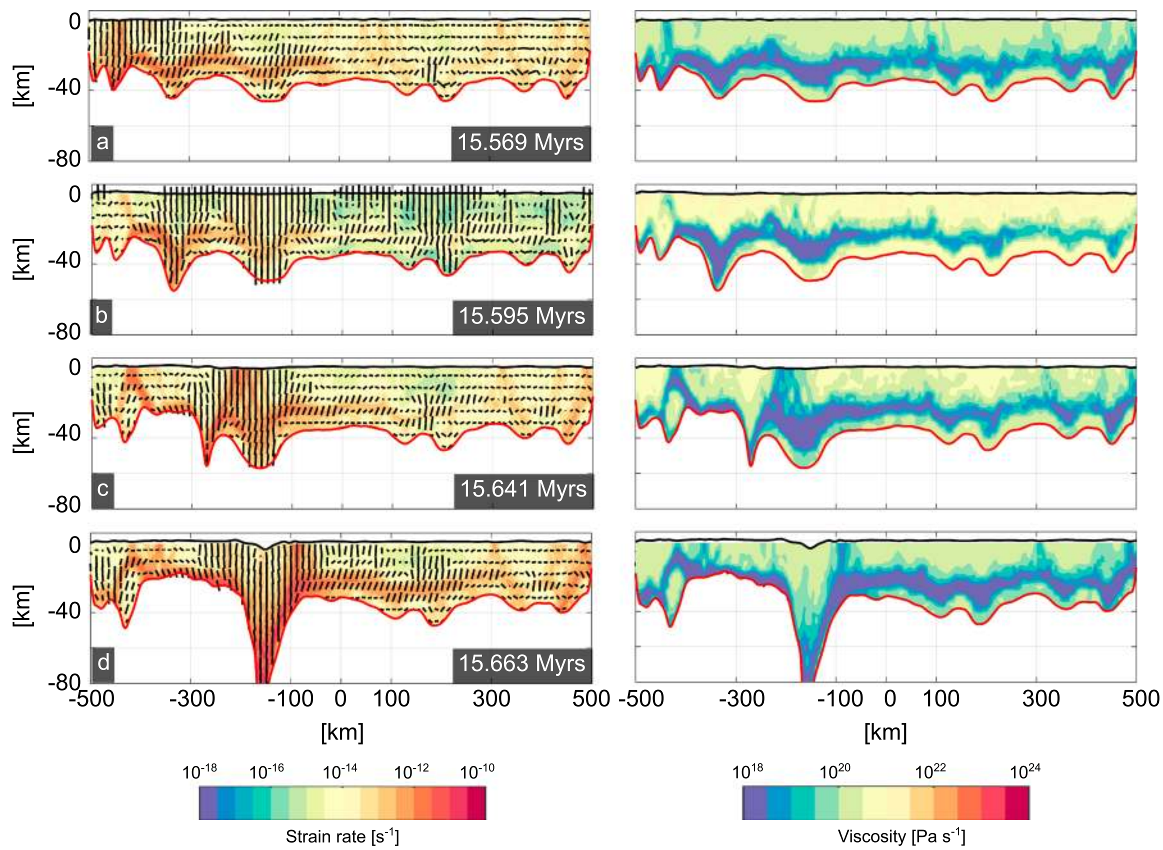

Figure 4. Strain rate and viscosity field The left and right column represent strain rate and viscosity field, respectively, of the crust. The thick black and red lines are the topography and the Moho, respectively. At the top of the strain rate field, the minimum axis of the stress tensor (σ_3) is shown. (a) After the first drip, the stress is propagated through the entire section of the crust, which concurrently helps to develop the adjacent drip and generates short-lived crustal scale shear zones in the right part of the box. (b) The second drip starts enucleating, dragging the adjacent material. The stress field rotates generating extension in the left area and dragging dense material from the middle crust of the adjacent area. (c) After the delamination of the second drips, the asthenosphere upwells to fill the empty space left, generating melting that further weakens the crust, triggering a symmetric extension that facilitates the development of the third instabilities (whose density and metamorphic evolution is shown in Figures 2 and 3). (d) The extension propagates, assisted by drag force exerted by the asthenosphere and by the complete development of the third drips.

asthenosphere undergoes partial melting as a consequence of the high T_P. Melt is extracted from the uppermost partially melted area, and the mantle depleted residue sinks, generating small convective cells within the partially molten area of the asthenosphere (see Figure 2a) . These convection cells locally induce decompression melting that generates further mafic intrusive and eruptive material. Heat is mainly provided to the crust by the emplacement of stalled magmas and generates warm geotherms, consistent with those recorded in Meso-Archean terranes (Brown, 2007). By contrast, the radiogenic heat production has a smaller effect at this stage due to the paucity of relatively radiogenic felsic crust, which has been shown to play a major role for the generation of significant amount of continental crust (Bodorkos et al., 2006). Burial of hydrated lavas following continued eruptions stabilizes amphibolite, garnet amphibolite, and garnet granulite with depth (Figures 1 and 3), which form at approximately 16-, 30-, and 36-km depths in the crust, respectively. Representative densities of each lithology along these geotherms comprise 3050–3150,3250–3300 and 3450–3550 kg/m^3, respectively. Both garnet amphibolite and garnet granulite melt to produce TTG-like magmas with major and trace element signatures matching Archaean examples. The burial is mainly controlled by the distribution of the magmatic activity that is focused beneath small convection cells in the asthenosphere. The mafic intrusions heat up the crust, driving the production and extraction of felsic magmas from amphibolite/garnet-amphibolite (hydrated metabasalt) and leaving a complementary mafic residuum. This process allows RTIs to develop (Figure 3b).

Partial melting of amphibolite/garnet-amphibolite followed by melt extraction generates large volumes of negatively buoyant mafic/ultramafic residue (Figure 3), which forms drips in thickened crust (Figure 3b).

Increased pressure in these regions acts to further stabilize garnet and destabilize feldspar, causing their sagging bases to transform to eclogite upon reaching pressures of ∼1.8 GPa, (Figures 3c and 3d). Further melting of these relatively dry eclogitic residual rocks is limited, consistent with observations that TTGs derived from eclogite-facies precursors represent minor (<10%) components of all Archean terrains (Moyen, 2011). During the incubation stage, the crust is weakened due to two factors: continuous emplacement of mafic intrusions that heats the lithosphere and the production of mafic (high-density) residuum, which destabilizes the entire lower-middle crust (see Figures 3 and 4b, where it is shown the density and viscosity field, respectively).

The *dripping stage* (∼14–22 Myr) starts as soon as the first drip nucleates, as shown in our simulations at the left-hand side of the numerical domain (Figure 4). The relatively high viscosity of the lithosphere enables the transmission of the gravitational pull force to the whole crust, which yields plastically due to weakening by magma percolation. The formation of drips allows asthenospheric mantle upwelling, which produces mafic melt that intrudes into and further weakens the crust. The crust is rafted apart by the asthenosphere and its horizontal displacement facilitates the nucleation of adjacent RTIs, enhancing the local compression associated with their development (Beall et al., 2017; Elkins-Tanton, 2007; see Figure 4). Local vertical stretching further increases the density of residual rocks (see Figure 3). The rapid evolution of the drips drags in the lower-middle crustal rocks from the adjacent area, whose migration locally induces intraplate extension near the drips (see Figure 4). The viscosity of the crust is sufficiently high to couple the buoyant mafic crust and the dense residual rocks. Brittle deformation controls the amount of material that can be dragged by the drips; since during the incubation-dripping stage the friction angle is decreased by the percolating mafic magmas, large amounts of composite material founders into the mantle (felsic and hydrous components). The dripped composite crust sinks and stalls at the bottom of the model, generating thermal/compositional anomalies.

The prolonged stretching of the crust generates narrow 2-D rift-like structures in which asthenosphere penetrates the crust. These processes result in a lateral variation in crustal structure coincident with felsic composition anomalies, which strongly resemble observed Archean dome and keel tectonic architecture (Figure 2; Bouhallier et al., 1995; Collins et al., 1998; Hamilton, 2007). The drip stage lasts 8 Myr, during which the proportion of felsic components increases to an average volume of 12% and up to 25% in the stretched region (with a production rate of 696 $km^3 \cdot km^{-1} \cdot Myr^{-1}$). Since significant amounts of cold volcanic crust are erupted at the surface, the resulting geotherm has a cold upper crust and hot lower crust, while the mantle T_P cools significantly by around 120 °C, producing a new ambient temperature of 1430 °C (see supporting information Figure S2). Importantly, the asthenospheric mantle becomes well mixed with residual and intrusive crustal components, which could allow partial hydration of the mantle that could trigger further melting (Bédard, 2006; Bédard et al., 2013); however, this process is not considered here. Intraplate deformation associated with the dripping stage is analogous to that proposed for the disaggregation of the Superior Craton, with our model providing a mechanism through which Archean lithosphere is weakened and rafted apart by mantle processes (Bédard & Harris, 2014; Bédard, 2018).

As a consequence of the dripping stage, the mantle cools, reducing its fertility, and its viscosity increases, making convection less efficient. While the crustal geotherm is cold as a consequence of the intense and fast magmatic thickening, resulting in a stiff crust (akin to the heat-pipe model; Moore & Webb, 2013). These conditions inhibit dripping, which is confined to the lowermost crust. These lower crustal drips are small compared to the initial one and have only minor geodynamic effects. The compositional evolution of the crust reaches a *steady state stage*, in which the felsic crust proportion steadily increases, concurrent with slow minor dripping of the mafic residuum. During the steady state stage, the mantle magmatic activity is no longer continuous and magma production is associated with small mantle upwellings triggered by the old dripped material that has become buoyant as consequence of its thermal equilibration. The original lithospheric mantle has been completely eroded, which makes the new crust virtually unsubductable (Bédard, 2018).

2.3.3. Sensitivity to the Initial Rheological Structure and Intrusive/Effusive Ratio

The initial rheological structure of the lithosphere affects the evolution of the numerical experiments. Increasing T_{Moho} weakens the crust and lithosphere because the respective geothermal gradient increases, and the viscosity decreases as a result. If the viscosity is low, the dense material in the lower-middle crust is fully decoupled from the buoyant supracrustal units. As a consequence the gravitational pull exerted by the RTIs is not effective, and the intraplate deformation observed in the reference experiment is suppressed,

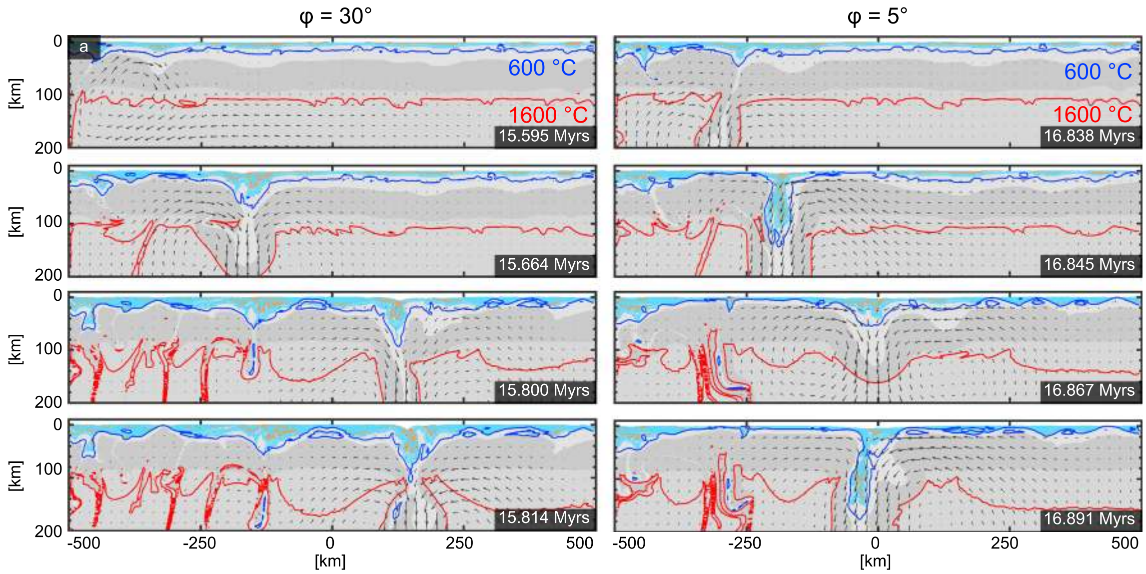

Figure 5. Effect of the strength of the crust on bringing hydrated material in the mantle. In these simulations, blue colors represent newly hydrated crust; orange, newly formed tonalite-trondhjemite-granodiorite; and gray, the lower crust, mantle lithosphere, and asthenosphere. The red and blue lines represent, respectively, the 600 and 1600 °C isotherms. Simulations are performed for a friction angle that is (a) similar to that of dry, intact crust and (b) represents that of a hydrated and damaged crust. Other parameters are the same as in the reference test (i.e., $T_{\mathrm{Moho}} = 800$ °C, $\lambda_{\mathrm{melt}} = 0.01$). Decreasing the friction angle results in a thinner crust and promotes periods of horizontal tectonics during which significant volumes of hydrated crust are transported into the mantle.

resulting in a lateral thickened and compositionally homogeneous crust (see supporting information Figures S3 and S4). Low brittle strength values ($\lambda_{\mathrm{melt}} < 0.1$, $\phi_{\mathrm{dry}} < 15°$) for the lithosphere favor intraplate deformation, drip formation, significant mantle cooling, and recycling of large amounts of variably hydrated mafic and felsic material into the mantle (Figure 5 and supporting information Figure S6). A strong lithosphere, on the other hand, has the opposite effect and results in a coherent lithosphere dominated by magmatic processes(see supporting information Figure S5).

The variation in the ratio between plutonism and volcanism does not significantly affect the four-stage evolution observed in the reference scenario unless more than 80% of mantle-derived magmas stall during ascent, in which case the total crustal recycling process is completed within 2 Myr. Retaining higher volumes of partial melt in the mantle (2% rather than 0.2%) decreases the timescales of the incubation stage (see supporting information Figures S7 and S8, which show the crustal thickness evolution).

2.3.4. Effect of T_P:

The duration of the incubation stage is inversely proportional to T_P. For example, at $T_P = 1450$ °C, the initial incubation stage lasts over 4 times longer than the reference scenario (65 Myr compared to 14 Myr). All dense lithologies (i.e., dry intrusion and mafic dense residuum, BS2–BS4) act in tandem to generate gravitational instabilities. The production of residuum facilitates the process by increasing the effective thickness of negatively buoyant material and favoring gravitational instabilities under a wide range of thermal conditions, especially at lower T_P. Before the onset of the drip instabilities, the ratio between new hot mantle-derived intrusions and mafic residuum is approximately 1:1, with the former being rheologically weaker and denser than mafic lower crust. This ratio grows in favor of the dense residuum as function of the T_{Moho}, the initial thickness and inversely respect with T_P. The amount of dense residuum required to trigger the drip instabilities in the reference scenario is 4 km (effective thickness, 12% of total crust thickness) with roughly the same amount of new dense intrusions. If the T_P (1450 °C) is lower, the amount of residuum is 8 km, meanwhile the amount of intruded material is halved compared to the reference scenario. The average volume of hydrous basalt that has depleted before the onset of the dripping stage thus gives a measure of the compositional evolution of the crust (see supporting information and Figure S2), as its maximum value represents how much of the hydrated crust has been converted while the crust was stable.

The average amount of metabasalt that must be converted into dense mafic residuum to trigger dripping instabilities monotonically increases with decreasing T_P (from 20% at 1550 °C to 72% at 1450 °C). Drips

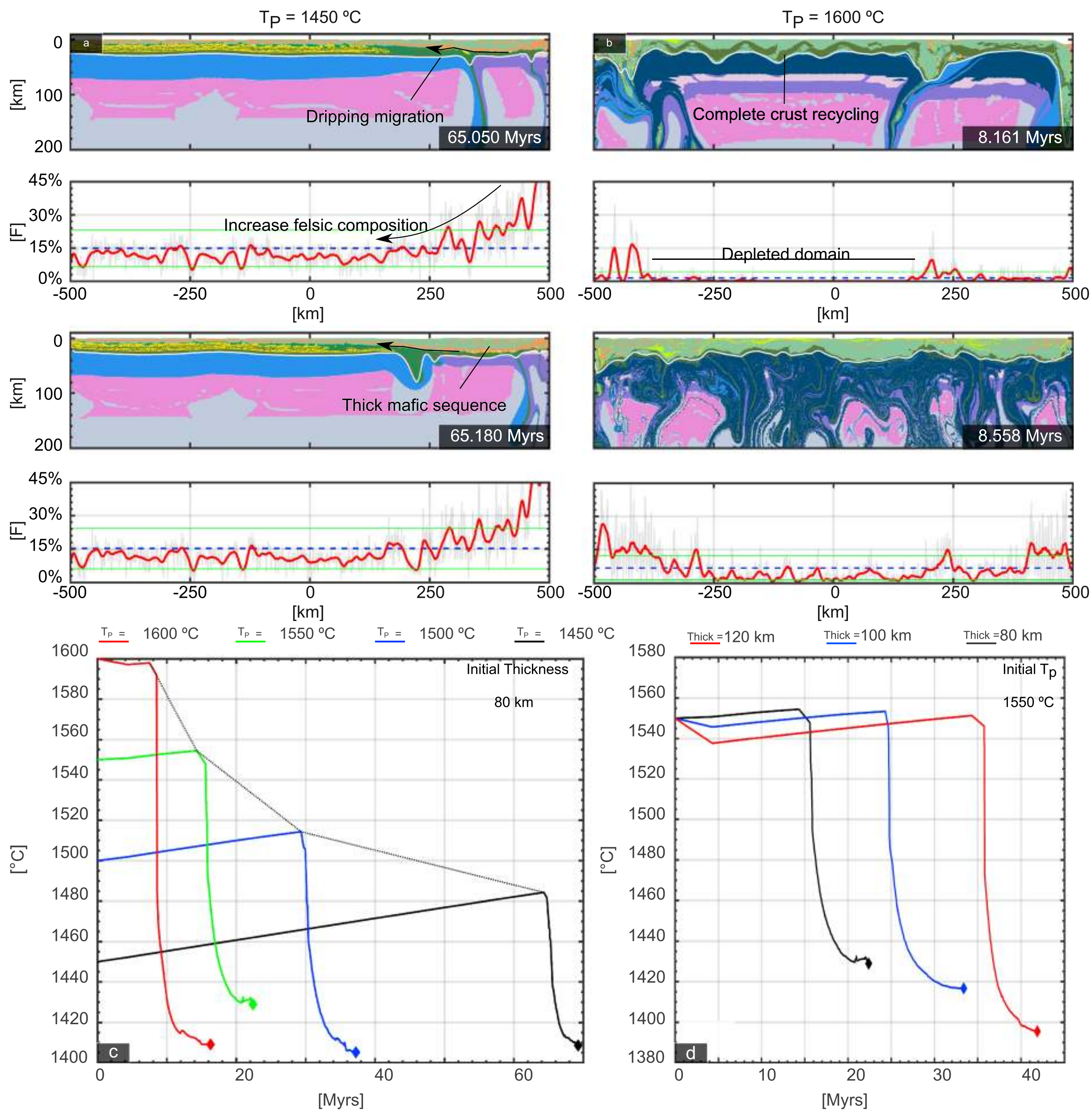

Figure 6. Effect of dripping instabilities on underlying mantle potential temperature (T_P). All the compositional plot use the same legend as in Figure 2. (a) Evolution of the dripping stage for an initial T_P of 1450 °C. A relatively low initial T_P prolongs the incubation stage, promoting the generation of significant volumes of felsic crust and associated dense, mafic residuum. Dripping is triggered by negative buoyancy and rheological weakening induced by the intrusion of hot mafic magmas. (b) As in (a), but with an initial T_P of 1600 °C. Here enhanced dripping causes the primitive crust to be completely recycled, regardless of the amount of felsic crust generated at any location. Multiple rifts develop simultaneously and enhance destruction of the primary mafic crust and derived felsic crust produced during the incubation stage. (c) Temporal evolution of average T_P for experiments with different initial T_P values (red, green, blue, and black lines represents experiment with an initial T_P of 1600, 1550, 1500, and 1450 °C, respectively). (d) Temporal evolution of experiments featuring the same T_P of 1550 °C but with different lithospheric thickness (black is 80 km, blue is 100 km, and red is 120 km). In all cases, the asthenospheric mantle T_P decreases rapidly as a result of addition of colder lithospheric material via dripping instabilities.

induced by such processes buffer the upper mantle T_P, such that localized mantle cool spots may have been present during the Archean associated with sites of TTG-like magma generation that immediately precede the drip (Figure 6). Higher initial mantle T_P (>1550 °C) promotes drip tectonics and total recycling of the crust without requiring large amounts of mafic dense residuum. The amount of intraplate deformation depends on the amount of extracted mafic melts and effectively ceases for mantle T_P values less than 1500 °C.

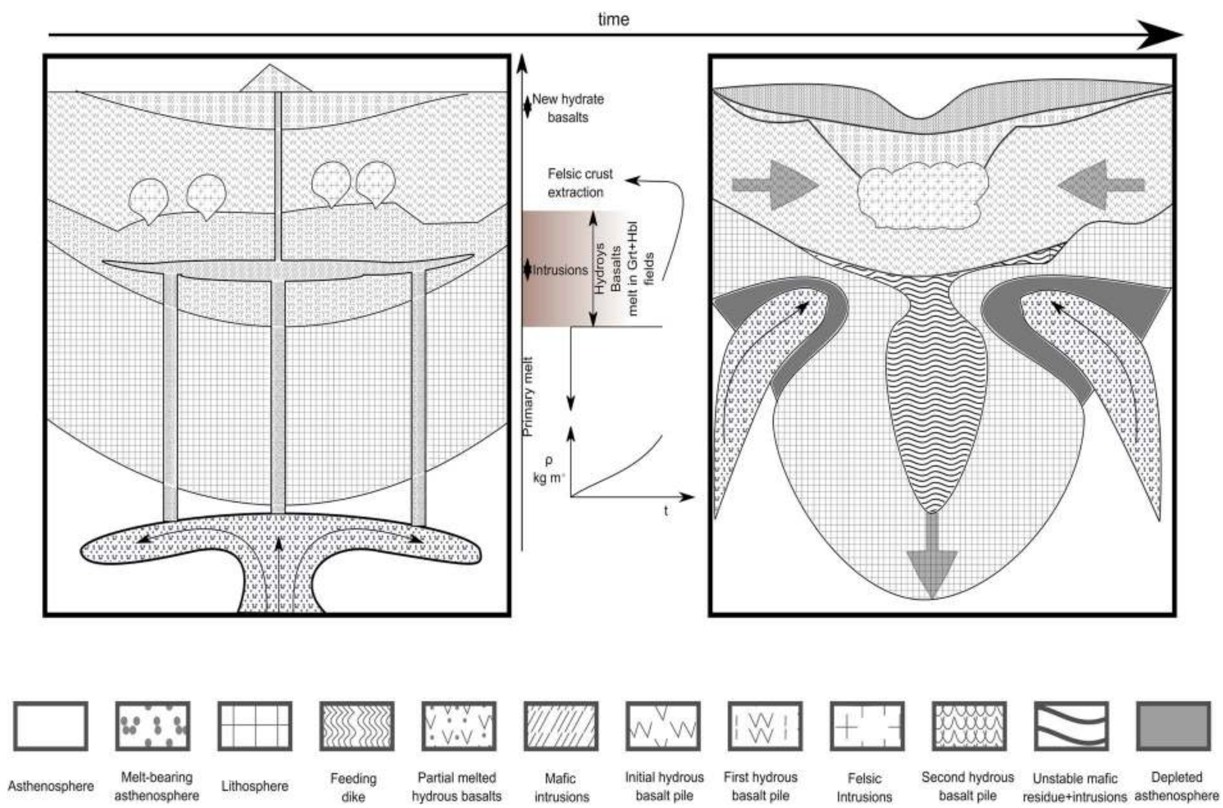

Figure 7. Simplified cartoon model. Melt coming from the astenosphere percolates through the lithosphere, heating and both plastically and thermally weakening it. Part of the mafic melts are emplaced in the lower crust, while the remnants are erupted. The thickness of the crust increases, while the thermal energy provided by the intrusions starts heating the previously generated hydrous crust, which melts producing large amounts of garnet enriched residuum. As soon as a critical amount of residuum is reached, RTIs are triggered, and asthenosphere fills the space left by the delaminated lithosphere. This results in a feedback between mantle melting and new crust production that enhances convection yielding a colder and depleted mantle.

2.3.5. Crustal Production Rates and Melting Conditions

The average amount of continental crust produced in these simulations during the incubation stage is 350 $\pm$ 280 $km^3 \cdot km^{-1} \cdot Myr^{-1}$, while during the dripping stage, the average production rate is 728 $\pm$ 254 $km^3 \cdot km^{-1} \cdot Myr^{-1}$ (see supporting information Figure S9). The continental crust production rate during the dripping stage does not correlate with the initial T_P, which only controls its rate of production during the incubation stage. The processes that control dripping-assisted continental crust production is mainly ruled by the feedback between asthenosphere decompression melting and the RTIs . The production of mafic melt is limited by the mantle depletion; thus, the independence from the T_P is related to the decreases of mantle fertility and by the extreme mantle cooling rate.

The *PT* conditions at which hydrated mafic crust experienced melting varied substantially during each experiment. In general, during the incubation stage TTG melt production is confined to low pressures, with a temperature gradient mainly controlled by the temperature of the intrusions. During the dripping stage, the thickness of the protomafic crust rapidly increases, shifting the melting conditions of the mafic protolith to higher pressures and temperatures, crossing the *PT* conditions necessary for producing TTG magmas with Archean major and trace element compositions shown by Palin et al. (2016). Our reference scenario features high-pressure melting conditions at the end of the dripping stage. However, the variability of the melt conditions and their median values depends strongly on the initial conditions (e.g., high T_{Moho} produce a horizontal homogenous thickened crust, which limits high-pressure TTGs). The ratio between mafic intrusion/extrusion exerts a strong control, and increasing it would result in a thinner crust that is completely outside the optimum field of TTGs generation. However, a slight increase (e.g., 65%) produces a perfect fit to the TTGs optimum field with respect to the reference scenario (see supporting information Figures S10, S11, and S13). TTGs have been classified in three categories: low pressure (LP, $0 < P < 1.0$ GPa), middle pressure (MP, $1.0 < P < 2.0$ GPa), and high pressure (HP, $P > 2.0$ GPa; Fischer & Gerya, 2016a; Moyen, 2011).

The classification is based on a global data set of TTGs and on the extensive experimental studies on TTGs generation (Moyen & Stevens, 2006). The three categories represents three different *PT* conditions in which TTGs might have been generated, in which the most important parameter is the pressure of generation. Such classification has been used to infer three different geodynamic settings to account TTGs production. The most abundant category is represented by the MP TTGs, 60% of all TTGs analyzed, while the other two represent 20% of the total TTGs analyzed (Moyen, 2011). The relative amount of these three type of TTGs have been widely used in geodynamical modeling to assess the proper condition of the TTGs generation (Fischer & Gerya, 2016a; Rozel et al., 2017). Yet the validity of this classification has been recently questioned using thermodynamic modeling (Palin et al., 2016), which demonstrate that the three types can be generated by prograde metamorphic paths over a much narrower pressure window. Our numerical experiments agree with Palin et al. (2016); however, if they are compared with the Moyen's (2011) classification, our model mostly are unable to replicate the distribution of the three categories. However, the model that most closely fits Moyen's (2011) classification is the one featuring the lowest I_R (i.e., 20%, see Figure S13). If I_R evolves during the whole experiments and accordingly the rheology of the crust, it is possible to cover the full gamut of conditions predicted by Palin et al. (2016) and Moyen (2011).

3. Discussion

The thermaltectonic effects of partial melting of an Archean mafic crust have been incorporated into two-dimensional numerical simulations of early-Earth geodynamics and show that drip tectonics can occur at even lower T_P than previously thought, owing to the concurrent emplacement of intrusions and production of garnet-rich mafic residuum via melting and melt loss. In our experimental framework, the mantle magmatic processes mostly control the rheological and density structure of the crust by heating it and producing felsic melts and complementary mafic dense residuum. Therefore, T_P control is indirectly exerted through the production of mafic magmas that fuel the process of continental crust production leading ultimately to RTIs. A colder T_P (<1550 °C) reduces the magmatic flux coming from the mantle, increasing the timescales of the incubation stage and increasing the importance of the mafic residuum on the dynamics of the experiment (see Figure 7 for a brief summary). Without the production of mafic dense residuum, the RTIs would not spontaneously form at this reduced T_P (Johnson et al., 2013) .

The large-scale geodynamic processes observed in our numerical experiments involving melting and foundering of the residue can be compared in some respects to those proposed for oceanic arcs (Jagoutz & Kelemen, 2015; Jagoutz, 2014), where the production of felsic crust via crystal fractionation of hydrated mafic parental magmas produces dense mafic cumulates. Both processes have similar consequences: the ultramafic cumulates and the residuum of the fractional crystallization founder back into the mantle leaving a crust enriched in felsic material (Behn et al., 2007). The operation of RTIs at present-day T_P highlights how they are an inevitable consequence of continental crust production and mantle magmatic processes. In the modern Earth, the mantle is partially molten in spatially restricted domains. Oceanic arcs are magmatically active as the subducting slab release fluids into the mantle triggering massive melting and reducing its viscosity (Behn et al., 2007; Schmidt & Poli, 1998), which jointly with the differentiation of mafic melts favors RTIs. However, this process would not trigger the feedback that induce a high felsic crust production and is different from drip-vertical tectonics (Bédard, 2006; Fischer & Gerya, 2016a; Zegers & van Keken, 2001). Our results predict that RTIs could have driven the generation of continental crust for the whole Archean, providing further support to the suggestion that has been made in previous numerical studies (Fischer & Gerya, 2016b; Sizova et al., 2015), and that dripping is associated with a rapid decrease of T_P. Lourenço et al. (2018) observed the same behavior in global scale geodynamical models and emphasized the role radiogenic heating has on the thermal history of rocky planets. Our results show that high mantle potential temperature could not last for long geological timescales and that the radiogenic heat affects the long-term stability of the lithosphere regardless of the initial T_P.

4. Conclusions

While a widely used estimate of Meso-Archaean mantle T_P of ∼ 1600 °C has been proposed based on calculated primary magma solutions for a small number of nonarc basalts (Herzberg et al., 2010), a more recent analysis of a significantly larger data set (22,000 samples) suggests that the Archean mantle may have had a lower T_P value of ∼ 1500 °C (Ganne & Feng, 2017). Our models show that large volumes of TTGs can be produced via crustal melting without requiring exceptionally high T_P and thus provide further support to the lowermost T_P estimates. Several studies argue that the average upper-mantle T_P could have been lower than the current estimation and invoke local temperature anomalies being responsible for rocks recording apparent high T_P (Arndt, 2013; Ganne & Feng, 2017; Kamber, 2015). However, metamorphic activity during the Archean seems to have been frequently punctuated by magmatic events, correlating with enhanced amounts of continental crust production, suggesting even fluctuations as function of the time (Bédard, 2018; Moyen & Van Hunen, 2012; O'Neill et al., 2015). These findings prompt the idea that regardless of the inherent variation of T_P, the thermal history of the Earth has not been monotonic (Condie et al., 2018; Davies, 1995; O'Neill et al., 2015; Sleep, 2000). It has been argued that such peak corresponds to plate tectonic activity to justify the production of continental crust (Moyen & Van Hunen, 2012; O'Neill et al., 2015), while our simulations demonstrate that dripping assisted continental crust production could be a viable alternative, consistent with the geological record. Therefore, variation of T_P either in space and time can potentially trigger this process while creating large amounts of felsic crust. The only requirement is that the whole upper mantle is sufficiently hot to produce mafic melts or that the crust bears sufficient amount of dense mafic residuum and intrusions (e.g., $T_P \geqslant 1450–1500\,^\circ$C). The Archean upper mantle could therefore not have featured a consistent T_P everywhere, supporting suggestions made from various independent lines of evidence for intermittent thermal histories on the early Earth in which fluctuations of T_P were associated explicitly with periodic mantle overturn (Condie et al., 2018; Davies, 1995) and with local variation of T_P associated with long-lasting plumes in a stagnant lid planet (Bédard, 2018).

Acknowledgments
We would like to thanks the Associate Editor, Taras V. Gerya, Jeroen Van Hunen, and Jean H. Bdard for the discussions and comment that improved our manuscript. This research has been supported by DFG grant, SPP 1833 Building a Habitable Earth and MAGMA Consolidator Grant (ERC project 71143). The numerical code and the reference test's initial setup can be downloaded at https://bitbucket.org/bkaus/mvep2/. The folder containing the reference test initial setup is inside the PROJECTS folder (Archean TTG). The script allows to reproduce the reference test simulation and to perform all the other experiments.

References

Anhaeusser, C. R. (2014). Archaean greenstone belts and associated granitic rocks—A review. *Journal of African Earth Sciences*, *100*, 684–732.

Arndt, N. T. (2013). The formation and evolution of the continental crust. *Geochemical Perspectives*, *2*(3), 405.

Beall, A. P., Moresi, L., & Stern, T. (2017). Dripping or delamination? A range of mechanisms for removing the lower crust or lithosphere. *Geophysical Journal International*, *210*(2), 671–692.

Bédard, J. H. (2006). A catalytic delamination-driven model for coupled genesis of Archaean crust and subcontinental lithospheric mantle. *Geochimica et Cosmochimica Acta*, *70*(5), 1188–1214.

Bédard, J. H. (2018). Stagnant lids and mantle overturns: Implications for Archaean tectonics, magmagenesis, crustal growth, mantle evolution, and the start of plate tectonics. *Geoscience Frontiers*, *9*(1), 19–49.

Bédard, J. H., Brouillette, P., Madore, L., & Berclaz, A. (2003). Archaean cratonization and deformation in the northern Superior Province, Canada: An evaluation of plate tectonic versus vertical tectonic models. *Precambrian Research*, *127*(1-3), 61–87.

Bédard, J. H., & Harris, L. B. (2014). Neoarchean disaggregation and reassembly of the Superior craton. *Geology*, *42*(11), 951–954.

Bédard, J. H., Harris, L. B., & Thurston, P. C. (2013). The hunting of the snArc. *Precambrian Research*, *229*, 20–48. https://doi.org/10.1016/j.precamres.2012.04.001

Behn, M. D., Hirth, G., & Kelemen, P. B. (2007). Trench-parallel anisotropy produced by foundering of arc lower crust. *Science*, *317*, 108–111.

Bodorkos, S., Sandiford, M., Benn, K., Mareschal, J., & Condie, K. (2006). Thermal and mechanical controls on the evolution of Archean crustal deformation: Examples from Western Australia. *GEOPHYSICAL MONOGRAPH-AMERICAN GEOPHYSICAL UNION*, *164*, 131.

Bouhallier, H., Chardon, D., & Choukroune, P. (1995). Strain patterns in Archaean dome-and-basin structures: The Dharwar craton (Karnataka, South India). *Earth and Planetary Science Letters*, *135*(1), 57–75. https://doi.org/10.1016/0012-821X(95)00144-2

Brown, M. (2007). Metamorphic conditions in orogenic belts: A record of secular change. *International Geology Review*, *49*(3), 193–234. https://doi.org/10.2747/0020-6814.49.3.193

Brown, M., & Johnson, T. (2018). Secular change in metamorphism and the onset of global plate tectonics. *American Mineralogist*, *103*(2), 181–196.

Cawood, P. A., Hawkesworth, C., & Dhuime, B. (2013). The continental record and the generation of continental crust. *Bulletin*, *125*(1-2), 14–32.

Chardon, D., Choukroune, P., & Jayananda, M. (1996). Strain patterns, décollement and incipient sagducted greenstone terrains in the Archaean Dharwar craton (south India). *Journal of Structural Geology*, *18*(8), 991–1004.

Chardon, D., Choukroune, P., & Jayananda, M. (1998). Sinking of the Dharwar basin (South India): Implications for Archaean tectonics. *Precambrian Research*, *91*(1-2), 15–39.

Choukroune, P., Bouhallier, H., & Arndt, N. (1995). Soft lithosphere during periods of Archaean crustal growth or crustal reworking. *Geological Society, London, Special Publications*, *95*(1), 67–86.

Clauser, C., & Huenges, E. (1995). Thermal conductivity of rocks and minerals. *Rock physics & phase relations*, *3*, 105–126.

Collins, W., Van Kranendonk, M. J., & Teyssier, C. (1998). Partial convective overturn of Archaean crust in the east Pilbara Craton, Western Australia: Driving mechanisms and tectonic implications. *Journal of Structural Geology*, *20*(9-10), 1405–1424.

Condie, K. C. (2003). Incompatible element ratios in oceanic basalts and komatiites: Tracking deep mantle sources and continental growth rates with time. *Geochemistry, Geophysics, Geosystems*, *4*(1), 1005. https://doi.org/10.1029/2002GC000333

Condie, K. C. (2005). High field strength element ratios in Archean basalts: A window to evolving sources of mantle plumes? *Lithos*, *79*(3-4), 491–504.

Condie, K. C., Aster, R. C., & van Hunen, J. (2016). A great thermal divergence in the mantle beginning 2.5 Ga: Geochemical constraints from greenstone basalts and komatiites. *Geoscience Frontiers*, *7*(4), 543–553.

Condie, K. C., Puetz, S. J., & Davaille, A. (2018). Episodic crustal production before 2.7 Ga. *Precambrian Research*, *312*, 16–22.

Cox, K. G. (1980). A model for flood basalt vulcanism. *Journal of Petrology*, *21*(4), 629–650. https://doi.org/10.1093/petrology/21.4.629

Crisp, J. A. (1984). Rates of magma emplacement and volcanic output. *Journal of Volcanology and Geothermal Research*, *20*(3-4), 177–211.

Cutts, K. A., Stevens, G., Hoffmann, J. E., Buick, I. S., Frei, D., & Münker, C. (2014). Paleo to Mesoarchean polymetamorphism in the Barberton Granite-Greenstone Belt, South Africa: Constraints from U-Pb monazite and Lu-Hf garnet geochronology on the tectonic processes that shaped the belt. *Bulletin*, *126*(3-4), 251–270.
Davies, G. F. (1995). Punctuated tectonic evolution of the Earth. *Earth and Planetary Science Letters*, *136*(3-4), 363–379.
Dhuime, B., Hawkesworth, C. J., Cawood, P. A., & Storey, C. D. (2012). A change in the geodynamics of continental growth 3 billion years ago. *Science*, *335*(6074), 1334–1336.
Elkins-Tanton, L. T. (2007). Continental magmatism, volatile recycling, and a heterogeneous mantle caused by lithospheric gravitational instabilities. *Journal of Geophysical Research*, *112*, B03405. https://doi.org/10.1029/2005JB004072
Fischer, R., & Gerya, T. (2016a). Early Earth plume-lid tectonics: A high-resolution 3D numerical modelling approach. *Journal of Geodynamics*, *100*, 198–214.
Fischer, R., & Gerya, T. (2016b). Regimes of subduction and lithospheric dynamics in the Precambrian: 3D thermomechanical modelling. *Gondwana Research*, *37*, 53–70.
Ganne, J., & Feng, X. (2017). Primary magmas and mantle temperatures through time. *Geochemistry, Geophysics, Geosystems*, *18*, 872–888. https://doi.org/10.1002/2016GC006787
Gerya, T. V. (2014). Precambrian geodynamics: Concepts and models. *Gondwana Research*, *25*(2), 442–463.
Gerya, T. V., & Meilick, F. I. (2011). Geodynamic regimes of subduction under an active margin: Effects of rheological weakening by fluids and melts. *Journal of Metamorphic Geology*, *29*(1), 7–31. https://doi.org/10.1111/j.1525-1314.2010.00904.x
Gerya, T., Perchuk, L., & Burg, J. P. (2008). Transient hot channels: Perpetrating and regurgitating ultrahigh-pressure, high-temperature crust–mantle associations in collision belts. *Lithos*, *103*(1-2), 236–256.
Green, E. C. R., White, R. W., Diener, J. F. A., Powell, R., Holland, T. J. B., & Palin, R. M. (2016). Activity composition relations for the calculation of partial melting equilibria in metabasic rocks. *Journal of Metamorphic Geology*, *34*(9), 845–869.
Hamilton, W. B. (2007). Earth's first two billion years the era of internally mobile crust. *Geological Society of America Memoirs*, *200*, 233–296.
Herzberg, C. T., Condie, K. C., & Korenaga, J. (2010). Thermal history of the Earth and its petrological expression. *Earth and Planetary Science Letters*, *292*(1-2), 79–88. https://doi.org/10.1016/j.epsl.2010.01.022
Hickman, A. H., & Van Kranendonk, M. J. (2012). Early Earth evolution: Evidence from the 3.5-1.8 Ga geological history of the Pilbara region of Western Australia. *Episodes*, *35*(1), 283–297.
Hirth, G., & Kohlstedt, D. (2004). Rheology of the upper mantle and the mantle wedge: A view from the experimentalists. *Inside the subduction Factory*, *138*, 83–105.
Holland, T. J. B., & Powell, R. (2003). Activity composition relations for phases in petrological calculations: An asymmetric multicomponent formulation. *Contributions to Mineralogy and Petrology*, *145*(4), 492–501.
Holland, T. J. B., & Powell, R. (2011). An improved and extended internally consistent thermodynamic dataset for phases of petrological interest, involving a new equation of state for solids. *Journal of Metamorphic Geology*, *29*(3), 333–383.
Jagoutz, O. (2014). Arc crustal differentiation mechanisms. *Earth and Planetary Science Letters*, *396*, 267–277.
Jagoutz, O., & Kelemen, P. B. (2015). Role of arc processes in the formation of continental crust. *Annual Review of Earth and Planetary Sciences*, *43*, 363–404.
Jahn, B. M., Glikson, A. Y., Peucat, J. J., & Hickman, A. H. (1981). REE geochemistry and isotopic data of Archean silicic volcanics and granitoids from the Pilbara Block, Western Australia: Implications for the early crustal evolution. *Geochimica et Cosmochimica Acta*, *45*(9), 1633–1652.
Johnson, T. E., Brown, M., Gardiner, N. J., Kirkland, C. L., & Smithies, R. H. (2017). Earth's first stable continents did not form by subduction. *Nature*, *543*(7644), 239–242.
Johnson, T. E., Brown, M., Kaus, B. J. P., & VanTongeren, J. A. (2013). Delamination and recycling of Archaean crust caused by gravitational instabilities. *Nature Geoscience*, *7*(1), 47–52. https://doi.org/10.1038/ngeo2019
Kamber, B. S. (2015). The evolving nature of terrestrial crust from the Hadean, through the Archaean, into the Proterozoic. *Precambrian Research*, *258*, 48–82.
Kaus, B. J. (2010). Factors that control the angle of shear bands in geodynamic numerical models of brittle deformation. *Tectonophysics*, *484*(1-4), 36–47.
Kaus, B. J. P., Mühlhaus, H., & May, D. A. (2010). A stabilization algorithm for geodynamic numerical simulations with a free surface. *Physics of the Earth and Planetary Interiors*, *181*(1-2), 12–20. https://doi.org/10.1016/j.pepi.2010.04.007
Kranendonk, M. J. V., Hickman, A. H., Smithies, R. H., Nelson, D. R., & Pike, G. (2002). Geology and tectonic evolution of the archean North Pilbara terrain, Pilbara Craton, Western Australia. *Economic Geology*, *97*(4), 695–732.
Kump, L. R., & Barley, M. E. (2007). Increased subaerial volcanism and the rise of atmospheric oxygen 2.5 billion years ago. *Nature*, *448*(7157), 1033–1036. https://doi.org/10.1038/nature06058
Lourenço, D. L., Rozel, A. B., Gerya, T., & Tackley, P. J. (2018). Efficient cooling of rocky planets by intrusive magmatism. *Nature Geoscience*, *11*(5), 322.
Martin, H., Moyen, J. F., Guitreau, M., Blichert-Toft, J., & Le Pennec, J. L. (2014). Why Archaean TTG cannot be generated by MORB melting in subduction zones. *Lithos*, *198-199*(1), 1–13. https://doi.org/10.1016/j.lithos.2014.02.017
Moore, W. B., & Webb, A. A. G. (2013). Heat-pipe Earth. *Nature*, *501*(7468), 501–505.
Moyen, J. F. (2011). The composite Archaean grey gneisses: Petrological significance, and evidence for a non-unique tectonic setting for Archaean crustal growth. *Lithos*, *123*(1), 21–36. https://doi.org/10.1016/j.lithos.2010.09.015
Moyen, J. F., & Martin, H. (2012). Forty years of TTG research. *Lithos*, *148*, 312–336.
Moyen, J. F., & Stevens, G. (2006). Experimental constraints on TTG petrogenesis: Implications for Archean geodynamics. In K. Benn, J.-C. Mareschal, & K. C. Condie (Eds.), *Archean geodynamics and environments* (Vol. 164, pp. 149–175). Washington, DC
Moyen, J. F., & Van Hunen, J. (2012). Short-term episodicity of Archaean plate tectonics. *Geology*, *40*(5), 451–454.
O'Neill, C., Lenardic, A., & Condie, K. C. (2015). Earth's punctuated tectonic evolution: Cause and effect. *Geological Society, London, Special Publications*, *389*(1), 17–40.
Palin, R. M., White, R. W., & Green, E. C. (2016). Partial melting of metabasic rocks and the generation of tonalitic–trondhjemitic–granodioritic (TTG) crust in the Archaean: Constraints from phase equilibrium modelling. *Precambrian Research*, *287*, 73–90.
Palin, R. M., White, R. W., Green, E. C., Diener, J. F., Powell, R., & Holland, T. J. (2016). High-grade metamorphism and partial melting of basic and intermediate rocks. *Journal of Metamorphic Geology*, *34*(9), 871–892.
Powell, R., & Holland, T. (1988). An internally consistent dataset with uncertainties and correlations: 3. Applications to geobarometry, worked examples and a computer program. *Journal of metamorphic Geology*, *6*(2), 173–204.
Ranalli, G. (1995). *Rheology of the Earth* (p. 413). London: Chapman and Hall.

Rapp, R. P., Shimizu, N., & Norman, M. D. (2003). Growth of early continental crust by partial melting of eclogite. *Nature*, *425*, 605–609. https://doi.org/10.1038/nature02031

Riel, N., Bouilhol, P., van Hunen, J., Cornet, J., Magni, V., Grigorova, V., & Velic, M. (2018). Interaction between mantle-derived magma and lower arc crust: Quantitative reactive melt flow modelling using STyx. *Geological Society, London, Special Publications*, *478*, SP478–6.

Rozel, A. B., Golabek, G. J., Jain, C., Tackley, P. J., & Gerya, T. V. (2017). Continental crust formation on early Earth controlled by intrusive magmatism. *Nature*, *545*, 47–52.

Rubin, A. M. (1993). Dikes vs. diapirs in viscoelastic rock. *Earth and Planetary Science Letters*, *119*(4), 641–659.

Rummel, L., Kaus, B. J., White, R. W., Mertz, D. F., Yang, J., & Baumann, T. S. (2018). Coupled petrological-geodynamical modeling of a compositionally heterogeneous mantle plume. *Tectonophysics*, *723*, 242–260.

Rushmer, T. (1995). An experimental deformation study of partially molten amphibolite: Application to low-melt fraction segregation. *Journal of Geophysical Research*, *100*(B8), 15,681–15,695.

Schmidt, M. W., & Poli, S. (1998). Experimentally based water budgets for dehydrating slabs and consequences for arc magma generation. *Earth and Planetary Science Letters*, *163*(1-4), 361–379.

Sizova, E., Gerya, T., & Brown, M. (2014). Contrasting styles of Phanerozoic and Precambrian continental collision. *Gondwana Research*, *25*(2), 522–545.

Sizova, E., Gerya, T. V., Brown, M., & Perchuk, L. L. (2010). Subduction styles in the Precambrian: Insight from numerical experiments. *Lithos*, *116*(3-4), 209–229. https://doi.org/10.1016/j.lithos.2009.05.028

Sizova, E., Gerya, T. V., Stüwe, K., & Brown, M. (2015). Generation of felsic crust in the Archean: A geodynamic modeling perspective. *Precambrian Research*, *271*, 198–224. https://doi.org/10.1016/j.precamres.2015.10.005

Sleep, N. H. (2000). Evolution of the mode of convection within terrestrial planets. *Journal of Geophysical Research*, *105*(E7), 17,563–17,578.

Thielmann, M., & Kaus, B. J. (2012). Shear heating induced lithospheric-scale localization: Does it result in subduction? *Earth and Planetary Science Letters*, *359*, 1–13.

Van Hunen, J., & Moyen, J. F. (2012). Archean subduction: Fact or fiction? *Annual Review of Earth and Planetary Sciences*, *40*, 195–219.

van Hunen, J., & van den Berg, A. P. (2008). Plate tectonics on the early Earth: Limitations imposed by strength and buoyancy of subducted lithosphere. *Lithos*, *103*(1-2), 217–235.

Van Kranendonk, M. J. (2010). Two types of Archean continental crust: Plume and plate tectonics on early Earth. *American Journal of Science*, *310*(10), 1187–1209.

Van Kranendonk, M. J., Hugh Smithies, R., Hickman, A. H., & Champion, D. (2007). Secular tectonic evolution of Archean continental crust: Interplay between horizontal and vertical processes in the formation of the Pilbara Craton, Australia. *Terra Nova*, *19*(1), 1–38.

White, S. M., Crisp, J. A., & Spera, F. J. (2006). Long-term volumetric eruption rates and magma budgets. *Geochemistry, Geophysics, Geosystems*, *7*, Q03010. https://doi.org/10.1029/2005GC001002

White, R., Powell, R., & Clarke, G. L. (2002). The interpretation of reaction textures in Fe rich metapelitic granulites of the Musgrave Block, central Australia: Constraints from mineral equilibria calculations in the system K_2O-FeO-MgO-Al_2O_3-SiO_2-H_2O-TiO_2-Fe_2O_3. *Journal of metamorphic Geology*, *20*(1), 41–55.

White, R. W., Powell, R., Holland, T. J. B., Johnson, T. E., & Green, E. C. R. (2014). New mineral activity composition relations for thermodynamic calculations in metapelitic systems. *Journal of Metamorphic Geology*, *32*(3), 261–286.

White, R. W., Powell, R., Holland, T. J. B., & Worley, B. A. (2000). The effect of TiO_2 and Fe_2O_3 on metapelitic assemblages at greenschist and amphibolite facies conditions: Mineral equilibria calculations in the system K_2O-FeO-MgO-Al_2O_3-SiO_2-H_2O-TiO_2-Fe_2O_3. *Journal of Metamorphic Geology*, *18*(5), 497–512.

Wiemer, D., Schrank, C. E., Murphy, D. T., Wenham, L., & Allen, C. M. (2018). Earth's oldest stable crust in the Pilbara Craton formed by cyclic gravitational overturns. *Nature Geoscience*, *11*(5), 357.

Wyman, D. (2013). A critical assessment of Neoarchean plume only geodynamics: Evidence from the Superior Province. *Precambrian Research*, *229*, 3–19.

Zegers, T. E., & van Keken, P. E. (2001). Middle Archean continent formation by crustal delamination. *Geology*, *29*(12), 1083–1086.